

Design of a digital, ultra-broadband electro-optic switch for reconfigurable optical networks-on-chip

Joris Van Campenhout, William M. J. Green, Yurii A. Vlasov

IBM T.J. Watson Research Center,
Yorktown Heights, NY 10598

jvancam@us.ibm.com

Abstract: We present a novel design for a noise-tolerant, ultra-broadband electro-optic switch, based on a Mach-Zehnder lattice (MZL) interferometer. We analyze the switch performance through rigorous optical simulations, for devices implemented in silicon-on-insulator with carrier-injection-based phase shifters. We show that such a MZL switch can be designed to have a step-like switching response, resulting in improved tolerance to drive-voltage noise and temperature variations as compared to a single-stage Mach-Zehnder switch. Furthermore, we show that degradation in switching crosstalk and insertion loss due to free-carrier absorption can be largely overcome by a MZL switch design. Finally, MZL switches can be designed for having an ultra-wide, temperature-insensitive optical bandwidth of more than 250 nm. The proposed device shows good potential as a broadband optical switch in reconfigurable optical networks-on-chip.

© 2009 Optical Society of America

OCIS codes: (130.4815) Optical switching devices; (250.6715) Switching

References and links

1. W. Bogaerts, P. Dumon, D. Van Thourhout, D. Taillaert, P. Jaenen, J. Wouters, S. Beckx, V. Wiaux, and R. G. Baets, "Compact wavelength-selective functions in silicon-on-insulator photonic wires," *IEEE J. Sel. Top. Quantum Electron.* **12**(6), 1394–1401 (2006).
2. F. N. Xia, M. Rooks, L. Sekaric, and Y. Vlasov, "Ultra-compact high order ring resonator filters using submicron silicon photonic wires for on-chip optical interconnects," *Opt. Express* **15**(19), 11,934–11,941 (2007).
3. F. Horst, W. M. J. Green, B. J. Offrein, and Y. Vlasov, "Echelle grating WDM (de-)multiplexers in SOI technology, based on a design with two stigmatic points," *Proc. SPIE* 6996, 69960R (2008).
4. Q. F. Xu, B. Schmidt, S. Pradhan, and M. Lipson, "Micrometre-scale silicon electro-optic modulator," *Nature* **435**(7040), 325–327 (2005).
5. W. M. J. Green, M. J. Rooks, L. Sekaric, and Y. A. Vlasov, "Ultra-compact, low RF power, 10 Gb/s silicon Mach-Zehnder modulator," *Opt. Express* **15**(25), 17,106–17,113 (2007).
6. M. Watts, D. Trotter, R. Young, and A. Lentine, "Maximally confined silicon microphotonic modulators and switches," in *Proceedings of the 21st Annual Meeting of the IEEE Lasers and Electro-Optics Society*, 457–458 (2008).
7. D. Ahn, C.-y. Hong, J. Liu, W. Giziewicz, M. Beals, L. C. Kimerling, J. Michel, J. Chen, and F. X. Krtnr, "High performance, waveguide integrated Ge photodetectors," *Opt. Express* **15**(7), 3916–3921 (2007).
8. G. Masini, S. Sahni, G. Capellini, J. Witzens, and C. Gunn, "High-Speed Near Infrared Optical Receivers Based on Ge Waveguide Photodetectors Integrated in a CMOS Process," *Adv. Opt. Technol.* 2008, 196572 (2008).
9. S. Assefa, F. Xia, S. W. Bedell, Y. Zhang, T. Topuria, P. M. Rice, and Y. A. Vlasov, "CMOS-Integrated 40GHz Germanium Waveguide Photodetector for On-Chip Optical Interconnects," in *Proceedings of OFC/NFOEC, OMR4* (2009).
10. J. Van Campenhout, P. Rojo-Romeo, P. Regreny, C. Seassal, D. Van Thourhout, S. Verstuyft, L. Di Cioccio, J. M. Fedeli, C. Lagahe, and R. Baets, "Electrically pumped InP-based microdisk lasers integrated with a nanophotonic silicon-on-insulator waveguide circuit," *Opt. Express* **15**(11), 6744–6749 (2007).

11. A. F. Benner, M. Ignatowski, J. A. Kash, D. M. Kuchta, and M. B. Ritter, "Exploitation of optical interconnects in future server architectures," *IBM J. Res. Dev.* **49**(4-5), 755-775 (2005).
12. T. Barwicz, H. Byun, F. Gan, C. W. Holzwarth, M. A. Popovic, P. T. Rakich, M. R. Watts, E. P. Ippen, F. X. Kartner, H. I. Smith, J. S. Orcutt, R. J. Ram, V. Stojanovic, O. O. Olubuyide, J. L. Hoyt, S. Spector, M. Geis, M. Grein, T. Lyszczarz, and J. U. Yoon, "Silicon photonics for compact, energy-efficient interconnects [Invited]," *J. Opt. Netw.* **6**(1), 63-73 (2007).
13. C. Batten, A. Joshi, J. Orcutt, A. Khilo, B. Moss, C. W. Holzwarth, M. A. Popovic, H. Q. Li, H. I. Smith, J. L. Hoyt, F. X. Kartner, R. J. Ram, V. Stojanovic, and K. Asanovic, "Building Many-Core Processor-to-DRAM Networks with Monolithic CMOS Silicon Photonics," *IEEE Micro* **29**(4), 8-21 (2009).
14. J. Ahn, M. Fiorentino, R. G. Beausoleil, N. Binkert, A. Davis, D. Fattal, N. P. Jouppi, M. McLaren, C. M. Santori, R. S. Schreiber, S. M. Spillane, D. Vantrease, and Q. Xu, "Devices and architectures for photonic chip-scale integration," *Appl. Phys. A* **95**(4), 989-997 (2009).
15. A. V. Krishnamoorthy, R. Ho, X. Z. Zheng, H. Schwetman, J. Lexau, P. Koka, G. L. Li, I. Shubin, and J. E. Cunningham, "Computer Systems Based on Silicon Photonic Interconnects," *Proc. IEEE* **97**(7), 1337-1361 (2009).
16. A. W. Poon, X. S. Luo, F. Xu, and H. Chen, "Cascaded Microresonator-Based Matrix Switch for Silicon On-Chip Optical Interconnection," *Proc. IEEE* **97**(7), 1216-1238 (2009).
17. A. Shacham, K. Bergman, and L. P. Carloni, "Photonic networks-on-chip for future generations of chip multi-processors," *IEEE Trans. Comput.* **57**(9), 1246-1260 (2008).
18. B. G. Lee, A. Biberman, P. Dong, M. Lipson, and K. Bergman, "All-optical comb switch for multiwavelength message routing in silicon photonic networks," *IEEE Photon. Technol. Lett.* **20**(9-12), 767-769 (2008).
19. Y. Vlasov, W. M. J. Green, and F. Xia, "High-throughput silicon nanophotonic wavelength-insensitive switch for on-chip optical networks," *Nat. Photon.* **2**(4), 242-246 (2008).
20. J. D. Owens, W. J. Dally, R. Ho, D. N. Jayasimha, S. W. Keckler, and L. S. Peh, "Research challenges for on-chip interconnection networks," *IEEE Micro* **27**(5), 96-108 (2007).
21. F. N. Xia, L. Sekaric, and Y. Vlasov, "Ultra-compact optical buffers on a silicon chip," *Nat. Photonics* **1**(1), 65-71 (2007).
22. J. Chan, A. Biberman, B. Lee, and K. Bergman, "Insertion loss analysis in a photonic interconnection network for on-chip and off-chip communications," in *Proceedings of the 21st Annual Meeting of the IEEE Lasers and Electro-Optics Society*, 300-301 (2008).
23. K. Barker, A. Benner, R. Hoare, A. Hoisie, A. Jones, D. Kerbyson, D. Li, R. Melhem, R. Rajamony, E. Schenfeld, S. Shao, C. Stunkel, and P. Walker, "On the Feasibility of Optical Circuit Switching for High Performance Computing Systems," in *Proceedings of the ACM/IEEE Supercomputing Conference*, p. 16 (2005).
24. K. Bergman, L. P. Carloni, J. A. Kash, and Y. Vlasov, "On-chip photonic communication for high-performance multi-core processors," in *Proceedings of the Eleventh Annual Workshop on High Performance Embedded Computing* (Lexington, MA, 2007).
25. I. Artundo, W. Heirman, M. Loperena, C. Debaes, J. Van Campenhout, and H. Thienpont, "Low-Power Reconfigurable Network Architecture for On-Chip Photonic Interconnects," in *Proceedings of 17th IEEE Symposium on High Performance Interconnects*, 163-169 (2009).
26. D. A. B. Miller, "Device Requirements for Optical Interconnects to Silicon Chips," *Proc. IEEE* **97**(7), 1166-1185 (2009).
27. R. A. Soref and B. R. Bennett, "Electrooptical Effects in Silicon," *IEEE J. Quantum Electron.* **23**(1), 123-129 (1987).
28. Y. Silberberg, P. Perlmutter, and J. E. Baran, "Digital Optical Switch," *Appl. Phys. Lett.* **51**(16), 1230-1232 (1987).
29. H. F. Hamann, A. Weger, J. A. Lacey, Z. G. Hu, E. Cohen, and J. Wakil, "Hotspot-limited microprocessors: Direct temperature and power distribution measurements," *IEEE J. Solid-State Circuits* **42**(1), 56-65 (2007).
30. E. Alon, V. Stojanovic, and M. A. Horowitz, "Circuits and techniques for high-resolution measurement of on-chip power supply noise," *IEEE J. Solid-State Circuits* **40**(4), 820-828 (2005).
31. M. Kuznetsov, "Cascaded Coupler Mach-Zehnder Channel Dropping Filters for Wavelength-Division-Multiplexed Optical-Systems," *J. Lightwave Technol.* **12**(2), 226-230 (1994).
32. R. C. Alferness and P. S. Cross, "Filter Characteristics of Co-Directionally Coupled Waveguides with Weighted Coupling," *IEEE J. Quantum Electron.* **14**(11), 843-847 (1978).
33. Y. P. Li and C. H. Henry, "Silica-based optical integrated circuits," *IEE Proc.-Optoelectron.* **143**(5), 263-280 (1996).
34. A. Takagi, K. Jinguji, and M. Kawachi, "Silica-Based Wave-Guide-Type Wavelength-Insensitive Couplers (Wincs) with Series-Tapered Coupling Structure," *J. Lightwave Technol.* **10**(12), 1814-1824 (1992).
35. K. Jinguji, N. Takato, A. Sugita, and M. Kawachi, "Mach-Zehnder Interferometer Type Optical Wave-Guide Coupler with Wavelength-Flattened Coupling Ratio," *Electron. Lett.* **26**(17), 1326-1327 (1990).
36. T. Kitoh, N. Takato, K. Jinguji, M. Yasu, and M. Kawachi, "Novel Broad-Band Optical Switch Using Silica-Based Planar Lightwave Circuit," *IEEE Photon. Technol. Lett.* **4**(7), 735-737 (1992).
37. S. M. Sze, *Physics of Semiconductor Devices* (J. Wiley and Sons, New York, 1982).
38. S. K. Selvaraja, W. Bogaerts, P. Dumon, D. Van Thourhout, and R. G. Baets, "Subnanometer Linewidth Unifor-

mity in Silicon Nanophotonic Waveguide Devices Using CMOS Fabrication Technology,” accepted for publication in IEEE J. Sel. Top. Quantum Electron.

39. J. T. Robinson, K. Preston, O. Painter, and M. Lipson, “First-principle derivation of gain in high-index-contrast waveguides,” *Opt. Express* **16**(21), 16,659–16,669 (2008).
 40. E. D. Palik, *Handbook of Optical Constants of Solids* (Academic, London, 1985).
-

1. Introduction

Over the past decade, impressive progress has been made in the field of silicon photonics, witnessed by the demonstration of silicon-based, passive optical devices such as wavelength-division-multiplexing (WDM) filters [1]-[3], as well as active devices such as high-speed silicon modulators [4]-[6], silicon-integrated germanium detectors [7]-[9] and hybrid silicon-III-V laser diodes [10]. As a result, short-range optical interconnects based on silicon are being considered as a promising technology for alleviating the chip-level interconnection bottleneck, anticipated in future, massively parallel computing systems [11, 12]. Optical network-on-chip (ONoC) architectures capable of providing reconfigurable communication paths between the processor cores and memory systems on a chip multiprocessor have been proposed [13]-[17]. In order to obtain an ONoC with sufficiently high bandwidth capacity, the use of aggressive wavelength-division multiplexing (WDM) is believed to be inevitable. The proposed ONoC architectures include both approaches using wavelength-selective routing schemes [13]-[16], as well as non-wavelength-selective implementations [17].

A key device for non-wavelength-selective ONoC architectures as proposed in [17] is the broadband optical switch, capable of routing an optical data stream encoded in multiple parallel wavelength channels. Previously, resonant, ring-based optical switches have been proposed for routing such data streams in on-chip interconnection networks [6, 18, 19]. Alternatively, non-resonant switches based on a Mach-Zehnder (MZ) interferometer could be used for this purpose. The non-resonant interference mechanism inherent to such devices is ideally suited to enable spectrally broadband operation, as well as temperature-insensitive switching.

In this paper, we analyze the performance of MZ-based electro-optic switches in silicon, based on carrier injection in a p-i-n diode phase shifter. First, in section 2, we review the switch requirements for a non-wavelength-selective ONoC. We emphasize the need for a digital switching response, which enhances the tolerance to drive-voltage noise and temperature variations, as well as the need for a wide optical switch bandwidth, which enhances the throughput capacity of the network. Next, in section 3, we assess the switching performance of the conventional single-stage MZ electro-optic switch and outline some of its shortcomings with respect to the previously identified device requirements. Subsequently, in sections 4 and 5, we propose a novel switch design based on a multi-stage Mach-Zehnder lattice (MZL), which has a largely improved tolerance to drive-voltage noise owing to its step-like switching response, as well as a substantially larger optical bandwidth. In section 6, we discuss and quantify the tolerance against voltage noise and temperature variations of the proposed switches. In section 7, we briefly discuss the tolerance against fabrication imperfections. Finally, in section 8, we summarize the device performance of the various switch designs and draw a conclusion.

2. Device requirements for broadband switches in a reconfigurable ONoC

2.1. Optical bandwidth and crosstalk

The required core-to-core communication bandwidth in future multicore processors is expected to be on the order of a few Tbps, while the clock rate anticipated in such systems is in the range 5-10GHz [20]. As such, it is unlikely that the data rate of an individual optical channel in the proposed ONoC will exceed 10 to 20 Gbps. Therefore, WDM schemes with a large number of

wavelength channels will have to be employed, in order to reach the desired aggregate core-to-core data rates while keeping the number of parallel waveguides between cores manageable. At the same time, the WDM channel spacing should not be too aggressive, in order to enable WDM filters with reasonable tolerance against temperature variations and fabrication imperfections [2, 21]. Therefore, the optical switches implemented in non-wavelength-selective ONoCs should preferably have a very wide optical bandwidth, allowing for a large number of coarsely spaced WDM channels to be simultaneously routed by a single switch. Assuming a channel spacing of 2 nm and a single-channel data rate of 10 Gbps, an optical bandwidth of 200 nm or more would be required for routing a 1-Tbps data stream in a single waveguide.

In order to avoid communication errors due to crosstalk from aggressor channels at any given receiver in the ONoC, the switches at the nodes of the ONoC should have crosstalk levels well below the worst-case insertion loss of any optical path in the ONoC. This insertion loss has contributions from the waveguide propagation loss, the loss due to waveguide crossings and the insertion loss of the optical switches along the path, and can for reasonably sized ONoCs quickly add up to 10 dB and more [22]. As such, in this paper, we require the switches to have a crosstalk level of -20 dB or lower, for both the 'on' and 'off' switch states.

2.2. *Switching speed, power and voltage*

A silicon-based optical switch with a switching speed in the nanosecond range is a key device for enabling flexible, circuit-switched optical interconnection fabrics [23] at the chip scale [17, 24]. The implementation of fast switches would enable the ONoC to quickly react to dynamically changing requests for communication bandwidth between the cores of a chip multi-processor (CMP). The implementation of a circuit-switched ONoC with a reconfiguration time in the range of a few tens to a few hundreds of nanoseconds could potentially result in substantial performance gains for many applications running on a CMP [17, 25].

The total energy budget for a complete on-chip optical interconnect is estimated to be 100 fJ/bit and lower [12, 26]. Therefore, the available energy budget for routing an optical bit through the ONoC will be a few tens of femtojoules per bit at most. Since an optical path in the ONoC may involve many active switches, the energy budget per bit and per switch will be most likely only a few femtojoules. For a broadband switch with a 1-Tbps throughput capacity, this is equivalent with a steady-state power consumption of a few milliwatts. The drive voltages should be compatible with the output voltages of drive circuits implemented in complementary oxide-semiconductor-metal (CMOS) technology, and should preferably be 1 V or less.

Given the requirements for speed, power and voltage, the preferred switching method is based on free-carrier injection in a forward-biased p-i-n diode [5, 27]. Phase shifters based on such diodes allow for large phase shifts to be obtained with short phase shifters and low drive voltage, and with switching speeds up to 10 GHz [5]. However, the use of phase shifters based on carrier injection into a p-i-n diode has implications for the crosstalk, insertion loss and noise tolerance of the switches, as we will discuss in this paper.

2.3. *Tolerance to noise: a digital switching response*

It is known that temperature fluctuations on a CMOS chip can be on the order of several tens of degrees, and that they typically appear as local hot spots [29]. Moreover, densely populated CMOS chips also suffer from power-supply noise, which can be as large as several tens of millivolts peak-to-peak [30]. Optical switches, integrated with CMOS circuits on the same chip, should be tolerant to such temperature and drive-voltage fluctuations.

A noise-tolerant switch is often referred to as a 'digital' optical switch [28]. Such a switch is designed to exhibit a step-like switching response as illustrated in in Fig. 1a, where the transmittance curves $T_{11}(V)$ and $T_{12}(V)$ are plotted as a function of drive voltage V . The transmittance

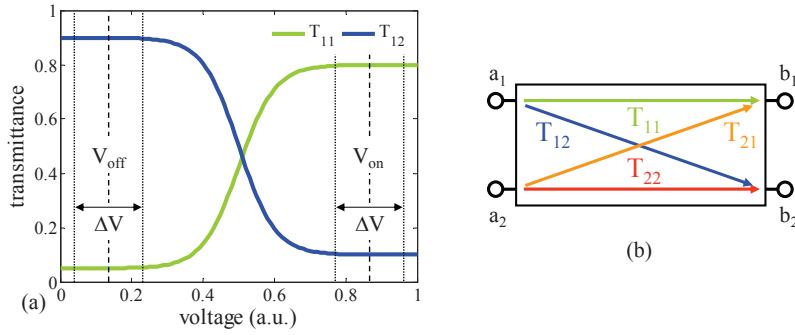


Fig. 1. (a) Example of a digital switching response [28], featuring a step-like transition from the ‘off’ to the ‘on’ state as a function of applied voltage. This step-like response provides tolerance against voltage noise ΔV , both for the ‘off’ as well as for the ‘on’ state. (b) The transmission coefficients T_{ij} are defined as the power transmittance from input port a_i to output port b_j .

curves $T_{ij}(V)$ are defined as $T_{ij}(V) = |S_{ij}(V)|^2$, where $S_{ij}(V)$ are the voltage-dependent, complex transfer functions of the optical field from input port a_i to output port b_j ($i, j = 1, 2$), as illustrated in Fig. 1b. The step-like switching response ensures tolerance against voltage fluctuations ΔV , both for the ‘off’ state of the switch, as well as for the ‘on’ state.

3. Review of the Mach-Zehnder switch

First, we review the switching response of a MZ switch, used here as a reference. The MZ interferometer is assumed to be balanced and to have two 50-% directional couplers (at the $1.55\text{-}\mu\text{m}$ design wavelength), as shown in Fig. 2a. The switch also contains a $500\text{-}\mu\text{m}$ -long p-i-n diode phase shifter. The switching response was evaluated by calculating the transmission coefficients $T_{ij}(\lambda, N) = |S_{ij}(\lambda, N)|^2$, where λ is the wavelength and N the density of free carriers, injected into the phase shifter by forward biasing the p-i-n diode. The transfer-matrix method was used for these simulations (see appendix for more details). In order to include the effect of both free-carrier dispersion (FCD), which provides the phase shift $\Delta\phi(N)$, as well as the effect of free-carrier absorption (FCA), which results in a propagation loss $\alpha(N)$, the real part as well as the imaginary part of the carrier-plasma effect was considered according to Soref’s empirical coefficients [27], at a wavelength of $1.55\text{ }\mu\text{m}$. Passive optical losses due to scattering and bending were not included. Therefore, any obtained insertion loss is completely due to FCA.

3.1. Switching response

First, the switching response was calculated at the design wavelength $\lambda = 1.55\text{ }\mu\text{m}$, as a function of the injected-carrier density. The result is shown in Fig. 2b. As expected, in the ‘off’ state ($N_{\text{off}} = 0$), the optical signal arriving at the input port a_1 (a_2) is fully transferred to the b_2 (b_1) output port (‘cross’ state). The ‘on’ state is obtained when a π phase shift is induced in the phase shifter ($N_{\text{on}} = 5 \times 10^{17}\text{ cm}^{-3}$), causing the optical input signal from a_1 (a_2) to destructively interfere at the b_2 (b_1) output port, and effectively switching it to the b_1 (b_2) output port (‘bar’ state). It should be noted that $T_{11} = T_{22}$ and $T_{12} = T_{21}$ as a result of the symmetry of the MZ switch.

With increasing phase delay, the MZ device switches back and forth between the ‘cross’ and the ‘bar’ state in a raised-cosine-like fashion, owing to the interference mechanism involving just two optical paths. Also, at higher injected-carrier densities, both crosstalk and insertion

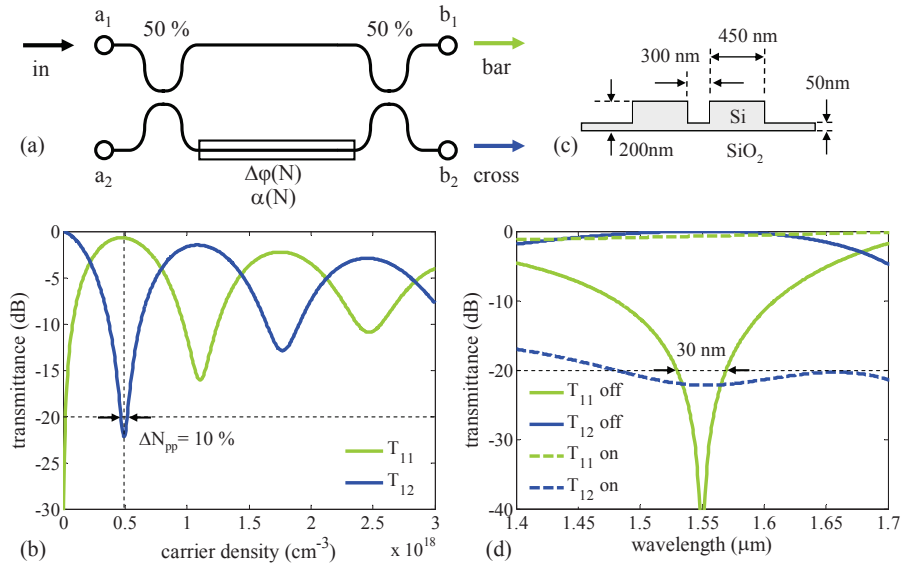


Fig. 2. (a) Schematic of the MZ switch, consisting of two 50-% couplers, with a 500- μm -long phase shifter based on a p-i-n diode. (b) Switching response of the MZ switch shown in (a) as a function of the density N of free carriers in the phase shifter. The ‘on’ state is reached for $N = 5 \times 10^{17} \text{ cm}^{-3}$, with a crosstalk of -22 dB and an insertion loss of 0.7 dB. The ‘on’-state noise tolerance ΔN_{pp} , -20 dB for maintaining -20 dB crosstalk is only 10 % (c) Cross section of the directional couplers (DC) used in the simulations. The silicon waveguides have $450 \times 200\text{-nm}^2$ cross-sectional dimensions including a 50-nm-thick bottom slab. The DC gap width is 300 nm. (d) Spectral switching response of the MZ switch using the DCs illustrated in (c), both for the ‘off’ state as well as for the ‘on’ state. The -20-dB optical bandwidth is only 30 nm.

loss increase, as a result of the increasing optical loss due to FCA in the phase shifter, which is sampled by 50% of the input light. For the ‘on’ state, the crosstalk is approximately -21.3 dB and the insertion loss is about 0.7 dB. While the ‘on’-state crosstalk could be reduced by push-pull operation or by adjusting the couplers to compensate for the FCA-related optical loss, this would result in higher ‘off’-state insertion loss and crosstalk.

The oscillatory nature of the MZ switching response is clearly in conflict with the requirement for having a digital switching response. The obtained crosstalk level is very sensitive to noise on the carrier density as a result of the analog switching response, as illustrated in Fig. 2b. It can be seen that ‘on’-state crosstalk levels of -20 dB can only be maintained if the relative peak-to-peak noise ΔN_{pp} , -20 dB on the injected-carrier density is kept below 10%. Such a tight ‘on’-state tolerance results in a weak tolerance to temperature and voltage fluctuations, for switches based on carrier injection in a forward biased p-i-n diode. Indeed, as we will discuss in section 6, a small variation ΔV on the voltage V_{on} applied to the diode in the ‘on’ state or a small temperature variation ΔT can result in a large variation ΔN of the injected-carrier density.

3.2. Optical bandwidth

In order to assess the optical bandwidth of the MZ switch, the transmission coefficients $T_{ij}(\lambda, N)$ were evaluated for wavelengths λ in the range 1.4-1.7 μm , both for the ‘off’ state ($N_{\text{off}} = 0$) and the ‘on’ state ($N_{\text{on}} = 0.5 \times 10^{17} \text{ cm}^{-3}$). These simulations included the wavelength dependence of the employed directional couplers (DC), as well as the first-order dispersion of

the effective index of the fundamental guided mode in the employed SOI rib waveguides. We assessed the optical bandwidth of the DCs by calculating their 100-% coupling length $L_C(\lambda)$ using a commercially available eigenmode-expansion tool. An analytical fit to these simulation results was consequently used in the wavelength-dependent transfer-matrix calculations (see appendix for more details). All simulations were done for transverse-electric (TE) polarization. The waveguides considered in these simulations were rib waveguides with 450×200 -nm² cross-sectional core dimensions, and a 50-nm thick lateral slab at the bottom of the waveguide core, which accommodates the p-i-n diode in the phase shifter. The waveguides were assumed to be embedded in SiO₂, and the width of the directional-coupler gap was fixed at 300 nm, as shown in Fig. 2c.

The resulting spectral switching response is shown in Fig. 2d. The optical bandwidth is mainly limited by crosstalk in the ‘off’ state, which is substantial for wavelengths strongly detuned from the 1.55- μ m design wavelength, due to imbalanced power splitting in the directional couplers. The optical bandwidth with -20-dB ‘off’-state crosstalk is about 30 nm. This bandwidth is clearly much lower than the 200-nm optical bandwidth desired for broadband switches in an ONoC application.

4. Design and simulation of a digital Mach-Zehnder lattice switch

The poor ‘on’-state noise tolerance obtained for the single-stage MZ switch can be improved by adding interferometric stages to the switch, essentially forming a Mach-Zehnder lattice (MZL) switch. The multiple interference paths available in a multi-stage MZL structure allow for engineering a more desirable, digital switching response, very much in analogy to the design of WDM filters based on MZL structures [31]. Furthermore, as we will show, the parasitic effect of FCA can be largely overcome with a MZL switch design, resulting in substantially lower crosstalk levels for the switch ‘on’ state as compared to the single-stage MZ switch.

The proposed switch consists of a Mach-Zehnder lattice containing S delay stages and $S + 1$ directional couplers with power coupling coefficients κ_i ($i = 1, 2, \dots, S + 1$), as illustrated in Fig. 3a. In the switch ‘cross’ (‘off’) state, the delay arms of each stage are balanced by design, and the coupling coefficients κ_i of the directional couplers are chosen such that all input light at a_1 is fully coupled to output port b_2 . In this configuration, the MZL can basically be considered as a discretized directional coupler (DC): the lengths of the individual DCs in every stage add up to the 100-% coupling length L_C of the employed DC. In order to switch the input light to the b_1 output port (‘bar’ or ‘on’ state) carriers are injected in the lower arms of each delay stage, causing a phase delay $\delta\phi(N)$ in the individual, identical phase shifters, for a total phase delay $\Delta\phi(N) = S\delta\phi(N)$. The operation principle can be considered as the discrete version of $\Delta\beta$ switching in a contiguous directional-coupler switch [32]: by creating a phase delay between the two arms, the optical beams going through the different optical paths no longer interfere constructively in the cross output waveguide and light is forced to stay in the input waveguide a_1 - b_1 .

4.1. MZL switches with uniform coupling coefficients

As a first example, we calculated the switching response of an MZL switch with $S = 8$ and uniformly distributed coupling coefficients ($\kappa_i = 3\%$). In order to allow straightforward comparison with the MZ switch, the aggregate length of the S phase shifters was again fixed at $L = 500 \mu\text{m}$, such that each individual phase shifter had a length of $L_S = L/S$.

The simulation results are shown in Fig. 3b. It can be seen that the oscillatory nature of the switching response is strongly reduced, when compared to the MZ switching response. Indeed, the MZL switching sidelobes are suppressed to less than -10 dB for carrier densities higher than the ‘on’-state carrier density $N_{\text{on}} = 8.2 \times 10^{17} \text{cm}^{-3}$. At the same time, the T_{11}

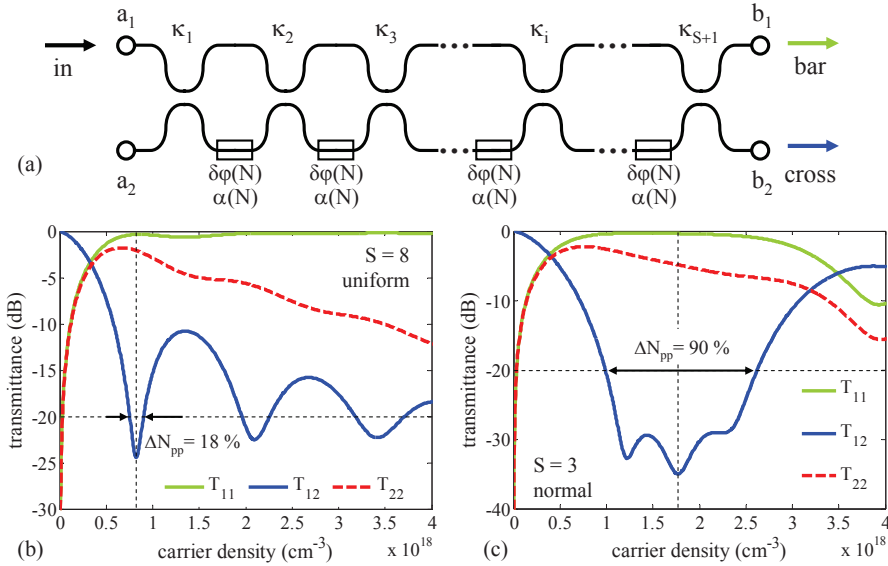


Fig. 3. (a) Schematic of the MZL switch, consisting of S interferometric stages, each having a coupling coefficient κ_i ($i = 1 \dots S + 1$) and a p-i-n diode providing a phase shift $\delta\phi(N)$. The total length of the individual diodes adds up to $500 \mu\text{m}$. (b) Switching response of an MZL switch with $S = 8$ and uniform coupling coefficients $\kappa_i = 3\%$. The ‘on’ state is reached for $N = 8.2 \times 10^{17} \text{cm}^{-3}$, with a crosstalk of -24dB and an insertion loss of 0.34dB . The noise tolerance $\Delta N_{\text{pp}, -20\text{dB}}$ is 18% . (c) Switching response of an MZL switch with $S = 3$ and normally distributed coupling coefficients ($\sigma = 0.5$). The ‘on’ state is reached for $N = 1.79 \times 10^{18} \text{cm}^{-3}$, with a crosstalk of -34dB and an insertion loss of 0.37dB . The noise tolerance $\Delta N_{\text{pp}, -20\text{dB}}$ is 90% .

insertion loss remains low, even for carrier densities as high as $N = 4 \times 10^{18} \text{cm}^{-3}$ (0.21dB), despite the substantial optical propagation loss $\alpha(N)$ induced in the phase shifters. As such, it is clear that the MZL design largely decouples the parasitic effect of FCA from the useful FCD effect, by preventing the majority of the input light from propagating in the lossy phase shifter(s). This results from the spatially distributed coupling along the MZL stages, with all individual coupling coefficients κ_i well below 50% . On the downside, the insertion loss for the T_{22} transmittance in the ‘on’ state has increased considerably to several decibels at high carrier densities, as all FCA loss is concentrated in the a_2 - b_2 waveguide. Therefore, an MZL switch is best used as a 1×2 switch. The best ‘on’-state crosstalk level reached at $N_{\text{on}} = 8.2 \times 10^{17} \text{cm}^{-3}$ is -24dB , and the ‘on’-state T_{11} insertion loss is 0.33dB , which are both slightly better as compared to the MZ switch. The noise tolerance $\Delta N_{\text{pp}, -20\text{dB}}$ is increased to about 18% .

The suppression of the switching sidelobes is essential for obtaining the desired digital switching response as shown in Fig. 1a. That said, the switching response obtained here is not digital in a strict sense, as the ‘off’-state crosstalk remains very sensitive to fluctuations of the injected-carrier density. However, as we will discuss in section 6, the rectifying behavior of the employed p-i-n diode phase shifter helps to enhance the noise tolerance in the ‘off’ state. As such, for the remainder of the paper, we focus on further reduction of the switching sidelobes, thereby increasing the tolerance of the MZL interferometer against noise in the ‘on’-state carrier density. This approach indeed results in MZL switches with a digital switching response as a function of the drive voltage, as we will show in section 6.

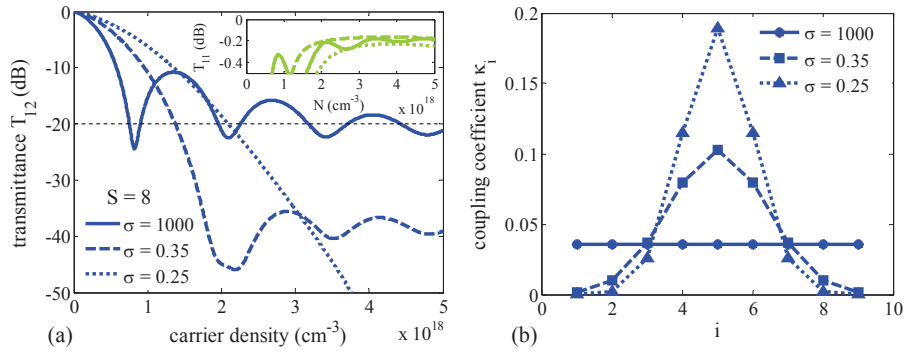


Fig. 4. (a) T_{12} switching response of three MZL switches with $S = 8$ and normally distributed coupling coefficients. The switching sidelobes can be suppressed to -10 dB, -36 dB and lower than -50 dB, for distribution variances $\sigma = 1000$, $\sigma = 0.35$ and $\sigma = 0.25$ respectively, as illustrated in (b). The inset in (a) shows the T_{11} switching response of the same devices. The 'on'-state insertion loss can be suppressed to lower than 0.2 dB.

4.2. MZL switches with apodized coupling coefficients

Apodizing the coupling coefficients of a passive, wavelength-selective MZL filter is a well-known technique to optimize its spectral response, for instance to reduce the amplitude of the spectral sidelobes of a channel-dropping WDM filter [31]. Simultaneous apodization of the coupling coefficient and phase mismatch along a directional-coupler switch is also known to produce $\Delta\beta$ switches with a digital switching response [32]. Typically, the apodization is done according to a window function, which can take uniform, normal, raised cosine, Hamming or other forms [32].

Likewise, the apodization technique can be equally beneficial for suppressing the switching sidelobes of the MZL switch. As the individual phase delays $\delta\phi(N)$ in the proposed MZL switch are all equal, the MZL switch belongs to the class of 'Fourier' filters [33]. As such, there exists a Fourier-transform relation between the switching response as function of the aggregate dephasing term $\Delta\phi(N) = L\Delta\beta(N)$, and the window function of the coupling coefficient.

As an example, we compared the response of the eight-stage, uniform MZL switch with the response of an eight-stage MZL switch with power coupling coefficients κ_i apodized according to a normal distribution

$$\kappa_i = \kappa_0 \exp \left[-\frac{1}{2} \left(\frac{i-1-S/2}{\sigma S/2} \right)^2 \right], \quad (1)$$

where σ^2 is the variance. The results for $\sigma = 0.25$ and $\sigma = 0.35$ are shown in Fig. 4a, with the respective coupling coefficients shown in Fig. 4b. It can be seen that the switching sidelobes can be strongly suppressed by decreasing the variance of the normal distribution. At the same time, both crosstalk and insertion loss are strongly reduced at these higher injection levels, as a result of the more adiabatic exposure of the input light to the lossy phase shifters. The 'on'-state T_{11} insertion loss for $\sigma = 0.25$ is reduced to less than 0.2 dB (inset of Fig. 4a) and the 'on'-state crosstalk can be lower than -50 dB.

Considering these results, it is clear that apodization of the coupling coefficients further suppresses the switching sidelobes, which helps to increase the 'on'-state noise tolerance. It also helps to further reduce the impact of FCA, yielding superior 'on'-state crosstalk and insertion loss. The main drawback of the apodization is the increase in carrier density required for switching.

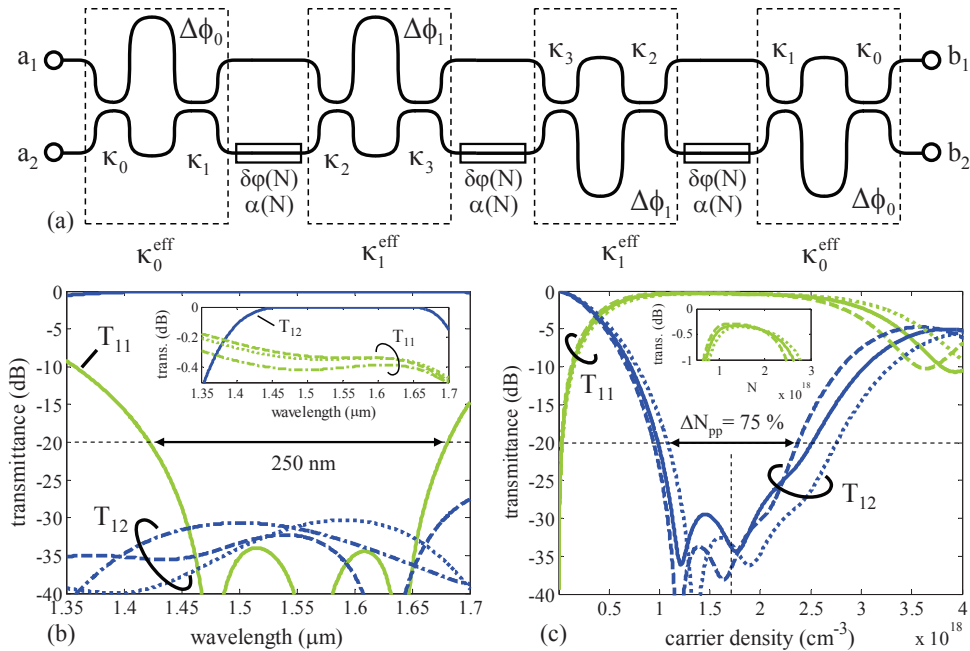


Fig. 5. (a) Schematic of the seven-stage WIMZL switch, which includes four passive, wavelength-insensitive coupling stages and three active phase-tuning stages. (b) Spectral switching response of the WIMZL switch with $(\kappa_0, \kappa_1, \Delta\phi_0) = (4.4\%, 10.6\%, 3.89)$ and $(\kappa_2, \kappa_3, \Delta\phi_1) = (58.2\%, 23.2\%, -4.06)$, for $N = 0$ (solid lines) and $N = 1.3, 1.6$ and $1.9 \times 10^{18} \text{ cm}^{-3}$ (dashed, dotted and dashed-dotted lines respectively). The -20-dB bandwidth is more than 250 nm . (c) Switching response versus carrier density N of the same WIMZL switch, for three different wavelengths ($\lambda = 1.45 \mu\text{m}, 1.55 \mu\text{m}$ and $1.65 \mu\text{m}$, in dashed, solid and dotted lines respectively). The noise tolerance $\Delta N_{\text{pp}, -20\text{dB}}$ is 75% , for all three wavelengths.

4.3. Low-order MZL switches

For many switching applications, it is of paramount importance to have low insertion loss. A real-world, high-order MZL switch could suffer from excessive (fabrication-related) insertion loss, as each stage will add losses due to the additional bending and linear propagation loss in these stages. Therefore, it is also worthwhile to investigate the potential benefits of an MZL switch with only a limited number of stages. As an example, we show the response of a three-stage MZL switch with normally distributed coupling coefficients ($\kappa_1 = 4.8\%$ and $\kappa_2 = 28.6\%$, $\sigma = 0.5$) in Fig. 3c. While the response of this low-order MZL has a substantial sidelobe at $N = 3.8 \times 10^{18} \text{ cm}^{-3}$, the ‘on’-state insertion loss for T_{11} is fairly low at 0.34 dB and ‘on’-state crosstalk is lower than -29 dB , for carrier densities in the range $N = 1.1 - 2.2 \times 10^{18} \text{ cm}^{-3}$. As such, the -29-dB noise tolerance $\Delta N_{\text{pp}, -29\text{dB}}$ is as high as 67% . The noise tolerance $\Delta N_{\text{pp}, -20\text{dB}}$ is 92% .

From these results, it is clear that the MZL design concept can be applied to obtain superior switching characteristics including reduced crosstalk and improved noise tolerance, while staying within the practical design constraints of device footprint and insertion loss.

5. Design and simulation of wavelength-insensitive Mach-Zehnder lattice switches

While the MZL switch design offers improved ‘on’-state switching characteristics, including improved noise tolerance and reduced crosstalk and insertion loss, the optical bandwidth is equally affected by the wavelength sensitivity of the employed DCs as for the case of the reference MZ switch. The bandwidth of these switches could be improved by either using broadband directional couplers with a reduced gap width, multimode-interference splitters, or specifically designed, tapered directional couplers [34]. Alternatively, the wavelength sensitivity of a single DC can be partially offset by a second DC, if a well chosen phase delay is implemented in between the couplers [35]. As such, some stages of the MZL switch could be dedicated to form wavelength-insensitive couplers, intermixed with the active phase tuning sections required for switching. The resulting device is a wavelength-insensitive MZL (WIMZL) switch.

As an example, we analyzed the performance of a seven-stage MZL switch with four passive stages and three active stages, as shown in Fig. 5a. The proposed WIMZL structure has point symmetry, which is essential to maximize the bandwidth of the switch [36]. In essence, the device behaves as a wavelength-insensitive, three-stage MZL switch with normally-distributed, effective power coupling coefficients κ_0^{eff} and κ_1^{eff} (4.8% and 28.6% respectively, $\sigma = 0.5$). First, the parameter sets $(\kappa_0, \kappa_1, \Delta\phi_0)$ and $(\kappa_2, \kappa_3, \Delta\phi_1)$ were optimized separately to yield the desired values for κ_0^{eff} and κ_1^{eff} in the 1.45–1.65- μm spectral window. This was done using MATLAB®’s genetic-algorithm toolbox `gatool` to minimize an error function, which was defined as the square of the deviation of the obtained coupling with the desired coupling, integrated over the targeted spectral window. The obtained values were then inserted in the matrix code describing the seven-stage structure and further fine-tuned for obtaining minimal crosstalk both for the ‘off’ and ‘on’ states, the latter being defined as $N = 1.3 - 1.9 \times 10^{18} \text{ cm}^{-3}$. The obtained values for $(\kappa_0, \kappa_1, \Delta\phi_0)$ and $(\kappa_2, \kappa_3, \Delta\phi_1)$ are (4.4%, 10.6%, 3.89) and (58.2%, 23.2%, -4.06) respectively.

The resulting spectral response is shown in Fig. 5b. The T_{11} and T_{12} transmittance spectra are shown for $N = 0$ (solid lines) and $N = 1.3, 1.6$ and $1.9 \times 10^{18} \text{ cm}^{-3}$ (dotted, dashed and dotted-dashed lines respectively). The WIMZ switch supports an ‘off’-state crosstalk level below -30 dB over a 200-nm-wide optical bandwidth, whereas an ‘off’-state crosstalk level below -20 dB can be maintained over a 250-nm-wide bandwidth (solid lines). ‘On’-state crosstalk levels are lower than -29 dB and T_{11} insertion loss is below -0.44 dB (see inset of Fig. 5b) for the same 250-nm bandwidth, and for carrier densities in the range $N = 1.3 - 1.9 \times 10^{18} \text{ cm}^{-3}$. Fig. 5c provides a further illustration of the switching response, showing the T_{11} and T_{12} transmittance curves as a function of injected carrier density, calculated for three different input wavelengths ($\lambda = 1.45 \mu\text{m}, 1.55 \mu\text{m}$ and $1.65 \mu\text{m}$, in dashed, solid and dotted lines respectively). For all three wavelengths, crosstalk levels are lower than -29 dB for carrier densities in the range $N = 1.23 - 1.99 \times 10^{18} \text{ cm}^{-3}$, reflecting a noise tolerance $\Delta N_{\text{pp}, -29\text{dB}} = 47\%$. For -20-dB crosstalk, the noise tolerance is as high as $\Delta N_{\text{pp}, -20\text{dB}} = 75\%$.

From these results, it is clear that the multiple optical interference paths available in a MZL structure can be exploited to obtain 1×2 carrier-injection-based switches with ultra-wide optical bandwidth, very low crosstalk levels and a robust tolerance against noise on the ‘on’-state carrier density, even for a relatively small number of interferometric stages.

6. Tolerance against voltage noise and temperature variations

6.1. Switching response as a function of applied voltage

As the phase shifters in MZL switches are preferably implemented as forward-biased p-i-n diodes, the switching response as function of applied forward voltage V will also depend on the N - V response of the diode. For an ideal p-i-n diode, this response is given by [37]

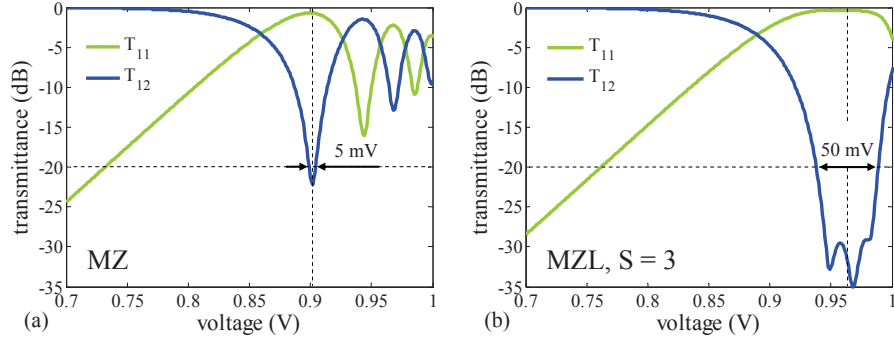


Fig. 6. (a) Switching response versus applied voltage for the MZ switch. The ‘on’-state voltage V_{on} is 0.9V. The noise tolerance $\Delta V_{\text{pp}, -20\text{dB}}$ is 5 mV. (b) Switching response of a MZL switch with $S = 3$ and $\sigma = 0.5$. V_{on} is approximately 0.96 V and $\Delta V_{\text{pp}, -20\text{dB}}$ is as high as 50 mV.

$$N(V, T) = N_i(T) \exp\left(\frac{qV}{2k_B T}\right) \sim T^{3/2} \exp\left(-\frac{E_g - qV}{2k_B T}\right), \quad (2)$$

where $N_i(T)$ is the temperature-dependent intrinsic carrier density in silicon, q is the elementary charge, k_B is the Boltzman constant and E_g is the bandgap of silicon. The switching response of the MZ switch as well as the response of an MZL switch with $S = 3$ and $\sigma = 0.5$ as introduced in section 4.3 were calculated as function of drive voltage V using equation (2) at room temperature ($T_0 = 300\text{K}$, $E_g = 1.12\text{eV}$, $N_i = 1.45 \times 10^{10}\text{cm}^{-3}$). The results are shown in Fig. 6. It can be seen that the ‘on’ state of the MZ switch is indeed highly sensitive to voltage noise: the maximum allowable peak-to-peak voltage noise $\Delta V_{\text{pp}, -20\text{dB}}^{\text{max}}$ for obtaining -20-dB crosstalk or better at a fixed temperature is only 5 mV, around the ‘on’-state voltage $V_{\text{on}} = 0.9\text{V}$. The noise tolerance of the MZL switch is ten times better with $\Delta V_{\text{pp}, -20\text{dB}}^{\text{max}} = 50\text{mV}$. It should also be noted that the expected ‘on’-state voltage $V_{\text{on}} = 0.96\text{V}$ of the MZL switch is only slightly larger than that of the MZ switch. Both switches have a high tolerance to ‘off’-state voltage fluctuations, as a result of the rectifying, exponential N - V response.

It is clear from expression (2) that the injected-carrier density will also depend on the diode temperature T . In general, the noise ΔN around a nominally injected-carrier density N_0 at a nominal voltage V_0 and temperature T_0 , caused by temperature fluctuations ΔT and voltage noise ΔV can be estimated to first order as

$$\frac{\Delta N}{N_0} = \frac{1}{300} (4.8 \times \Delta T + 0.6 \times 10^4 \Delta V), \quad (3)$$

where we assumed $T_0 = 300\text{K}$ and $V_0 = 0.95\text{V}$, and where ΔT is in Kelvin and ΔV is in Volt. From this equation, it is clear that the ‘on’-state noise budget ΔN_{pp} of a given device will affect both its ability to deal with on-chip temperature fluctuations as well as with on-chip voltage noise.

It should be noted that expression (2) doesn’t include the voltage drop due to the series resistance of a real-world diode, which is substantial at high diode currents. In the series-resistance-limited regime of the p-i-n diode, the N - V response is linear, and less sensitive to voltage fluctuations. As such, the tolerances to voltage and thermal noise calculated with Eq. (3) should be considered a worst-case estimation.

6.2. Thermal sensitivity of the optical response

Finally, temperature-insensitive operation also requires the optical response of the MZL switch to be thermally stable. In general, the temperature sensitivity of interference-based optical devices is determined by the variation of the coupling coefficients and the optical delay lengths with temperature. To first order, we can neglect the former contribution. For a design without built-in phase delay such as a symmetric MZ switch or MZL switch, the latter effect also vanishes, assuming that the spatial extent of on-chip thermal hotspots is much larger than the footprint of the switch. As such, these switches are optically temperature insensitive.

The ultra-broadband seven-stage WIMZL switch does include the phase delays $\Delta\phi_1$ and $\Delta\phi_2$ in its wavelength-insensitive coupling stages. However, the length imbalances $\Delta L_i = \Delta\phi_i\lambda_0/2\pi n_e^0$ to obtain these phase delays are small (less than $0.5\ \mu\text{m}$), and any additional phase imbalance due to temperature variations will be negligible (less than 0.02π , for a peak-to-peak temperature swing ΔT_{pp} of 100 K). From these considerations, and given the fact that the MZL switch is a non-resonant device, the optical response of the MZL switch design can also be considered as essentially temperature insensitive.

Table 1. Overview of the switching performance of various MZL switch designs

| | MZ | MZL | MZL | MZL | WIMZL |
|---|-------|-------------|-------------|-------------|-------------|
| S | 1 | 8 | 8 | 3 | 7 |
| window function | n/a | uniform | normal | normal | normal |
| σ | n/a | n/a | 0.35 | 0.5 | 0.5 |
| N_{on} ($10^{18}\ \text{cm}^{-3}$) | 0.5 | 0.82 | 2.2 | 1.79 | 1.73 |
| $\Delta\phi_{\text{on}}$ | π | 1.6π | 3.6π | 2.9π | 2.9π |
| XT_{on} (dB) | -22 | -24 | -46 | -34 | -33 |
| IL_{on} (dB) | 0.7 | 0.34 | 0.19 | 0.37 | 0.38 |
| $BW_{-20\text{ dB}}$ (nm) | 30 | 30 | 30 | 30 | 250 |
| $\Delta N_{\text{pp}, -20\text{ dB}}$ | 10% | 18% | 72% | 92% | 75% |
| $\Delta V_{\text{pp}, -20\text{ dB}}^{\text{max}}$ (mV) | 5 | 9 | 36 | 46 | 38 |
| $\Delta T_{\text{pp}, -20\text{ dB}}^{\text{max}}$ (K) | 6 | 11 | 45 | 58 | 47 |

7. Tolerance against fabrication imperfections

It is well known that the phase of a lightwave propagating in a submicron silicon waveguide is very sensitive to variations of the cross-sectional dimensions of the waveguide, owing to the tight mode confinement [38]. As a result, phase errors arising from variations in etch depth and waveguide width can accumulate quickly, especially along the longest optical delay paths of an interferometric device. It should be noted that the proposed (WI)MZL switch design doesn't directly enhance the ability to deal with such phase errors, making it equally prone to degradation in switching performance as compared to the reference MZ switch. The largest sensitivity to phase errors is most likely to occur in the p-i-n diode phase-shifter sections, as they comprise the longest optical paths along which relative phase errors can accumulate. As such, (WI)MZL switches with short phase shifters will most likely exhibit the best tolerance to fabrication imperfections. However, such devices will require comparably larger carrier densities for switching ($N_{\text{on}} > 2 \times 10^{18}\ \text{cm}^{-3}$), which most likely will require the utilization of p-i-n diode phase shifters with optimized electrical and thermal properties, capable of supporting these high carrier densities.

8. Summary and conclusion

An overview of the switching performance of the various switch designs presented in sections 3 to 5 is given in table 1. For each of the switch designs, the 'on'-state carrier density N_{on} is de-

defined as the carrier density that minimizes the crosstalk between T_{11} and T_{12} . Table 1 also gives an overview of the equivalent ‘on’-state phase delay $\Delta\phi_{\text{on}}$, as well as the obtained ‘on’-state crosstalk XT_{on} and the T_{11} insertion loss IL_{on} . The eight-stage MZL with normally distributed ($\sigma = 0.35$) coupling coefficients has the lowest XT_{on} (-46 dB) and lowest IL_{on} (0.19 dB). However, an MZL switch with only three stages and normally distributed ($\sigma = 0.5$) coupling coefficients already offers strongly improved XT_{on} (-34 dB) and IL_{on} (0.37 dB) as compared to the reference MZ switch ($\text{XT}_{\text{on}} = -22$ dB and $\text{IL}_{\text{on}} = 0.7$ dB). The reduction in crosstalk and insertion loss comes at the expense of a higher ‘on’-state carrier density, as well as a limitation to 1×2 switching functionality.

In order to compare the switch bandwidth of the various switch designs for an application requiring lower than -20-dB crosstalk, table 1 also gives an overview of the optical bandwidth $\text{BW}_{-20\text{dB}}$ for which -20-dB crosstalk is maintained, for both switching states. As already discussed in section 5, all MZ(L) switches have a $\text{BW}_{-20\text{dB}}$ of only 30 nm, whereas the WIMZL has a substantially wider optical bandwidth with $\text{BW}_{-20\text{dB}} = 250$ nm.

The noise tolerance is also summarized in table 1 for the various devices, by specifying the maximum allowable peak-to-peak carrier-density noise $\Delta N_{\text{pp}, -20\text{dB}}$ for maintaining -20-dB crosstalk. The MZL designs featuring coupling apodization exhibit an up to ninefold higher noise tolerance as compared to the MZ switch. Finally, the noise tolerance of the switches was further illustrated by using Eq. (3) to calculate their maximum allowable peak-to-peak temperature fluctuation $\Delta T_{\text{pp}, -20\text{dB}}^{\text{max}}$ without any voltage noise ($\Delta V = 0$), as well as the maximum allowable peak-to-peak voltage noise $\Delta V_{\text{pp}, -20\text{dB}}^{\text{max}}$ without any temperature fluctuations ($\Delta T = 0$), both evaluated for obtaining -20-dB crosstalk or better. As already mentioned, the reference MZ switch has very poor noise tolerance with $\Delta T_{\text{pp}, -20\text{dB}}^{\text{max}} = 6$ K and $\Delta V_{\text{pp}, -20\text{dB}}^{\text{max}} = 5$ mV, whereas the seven-stage WIMZL switch has much improved ‘on’-state noise tolerance $\Delta T_{\text{pp}, -20\text{dB}}^{\text{max}} = 47$ K and $\Delta V_{\text{pp}, -20\text{dB}}^{\text{max}} = 38$ mV.

In conclusion, we have proposed a novel ultra-broadband digital switch, based on a Mach-Zehnder lattice in silicon-on-insulator, and we have analyzed and optimized the response of such switches when implemented with carrier-injection based phase shifters. Such Mach-Zehnder lattice switches can be designed to have a digital switching response, which results in superior ‘on’-state crosstalk, insertion loss, as well as a drastically improved tolerance to thermal and drive-voltage noise, as compared to a single-stage MZ switch. By incorporating wavelength-insensitive coupling stages, their optical bandwidth can be improved to more than 250 nm, which would enable simultaneous switching of a large number of coarsely spaced WDM channels. While the switching performance improves with the number of employed stages, a MZL switch with a low number of stages already offers substantially improved switching characteristics over the MZ switch. Finally, the optical response of a MZL switch is insensitive to temperature fluctuations, which eliminates the need for power-hungry temperature stabilization. For the above reasons, we believe that the MZL switch has good potential as a broadband optical switch in a non-wavelength-selective circuit-switched ONoC.

Acknowledgments

This work was supported in part by the DARPA APS Program, under contract HR0011-08-C-0102. The views, opinions, and/or findings contained in this article are those of the authors and should not be interpreted as representing the official views or policies, either expressed or implied, of DARPA or the Department of Defense.

Appendix

Wavelength-dependent transfer-matrix calculations

We analyzed the switching characteristics of the proposed switches using the well-known transmission matrix formalism. The i -th coupler is described by the matrix $\mathbf{C}_i(\lambda)$

$$\mathbf{C}_i(\lambda) = \begin{bmatrix} t_i(\lambda) & jr_i(\lambda) \\ jr_i(\lambda) & t_i(\lambda) \end{bmatrix}, \quad (4)$$

where $r_i(\lambda)$ and $t_i(\lambda)$ are respectively given by

$$r_i(\lambda) = \sqrt{\kappa_i(\lambda)} \quad (5)$$

$$t_i(\lambda) = \sqrt{1 - \kappa_i(\lambda)}, \quad (6)$$

where $\kappa_i(\lambda)$ is the power coupling coefficient of the i -th coupler and $r_i^2(\lambda) + t_i^2(\lambda) = 1$, reflecting lossless coupling. The wavelength dependence of $\kappa_i(\lambda)$ is given by

$$\kappa_i(\lambda) = \sin^2 \left(\frac{\pi}{2} \frac{L_i^\kappa}{L_C(\lambda, g)} \right) \quad (7)$$

where $L_C(\lambda, g)$ is the wavelength-dependent 100-% coupling length of the directional coupler with gap width g , and L_i^κ relates to the nominally desired power-coupling coefficient κ_i of the i -th coupler at the design wavelength λ_0 as

$$L_i^\kappa = \frac{2L_C(\lambda_0, g)}{\pi} \arcsin(\sqrt{\kappa_i}). \quad (8)$$

The i -th *active* phase-tuning section is described by the transmission matrix $\mathbf{P}_i^A(\lambda)$:

$$\mathbf{P}_i^A(\lambda) = \begin{bmatrix} 1 & 0 \\ 0 & \exp[-j\Delta\beta(\lambda, N)L_S] \end{bmatrix}, \quad (9)$$

where L_S is the length of the individual phase sections and $\Delta\beta(\lambda, N)$ is the wavelength and carrier-concentration dependent perturbation of the propagation constant β , given by

$$\Delta\beta(\lambda, N) = \Gamma \frac{2\pi}{\lambda} \left[\Delta n(N) + \frac{j}{2} \alpha(N) \right]. \quad (10)$$

In Eq. (10), Γ is the effective optical confinement factor of the waveguide core [39]. Soref's empirical expressions [27] were used to quantify the free-carrier plasma dispersion effect, both including the real and imaginary part. Under the ambipolar assumption, $\Delta n(N)$ and $\alpha(N)$ are given by

$$\Delta n(N) = -8.8 \times 10^{-22} N - 8.5 \times 10^{-18} N^{0.8} \quad (11)$$

$$\alpha(N) = (8.5 \times 10^{-18} + 6 \times 10^{-18}) N, \quad (12)$$

reflecting the contributions from electrons and holes respectively. In these equations, N is expressed in $[\text{cm}^{-3}]$ and $\alpha(N)$ in $[\text{cm}^{-1}]$. For simplicity, these expressions were considered to be wavelength and temperature independent.

The i -th *passive* phase-tuning section is described by the transmission matrix $\mathbf{P}_i(\lambda)$:

$$\mathbf{P}_i(\lambda) = \begin{bmatrix} 1 & 0 \\ 0 & \exp[-j\beta(\lambda)\Delta L_i] \end{bmatrix}. \quad (13)$$

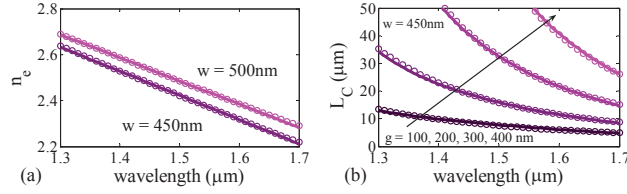


Fig. 7. Simulated (markers) and fitted (solid lines) model parameters $n_e(\lambda)$ (a) and $L_C(\lambda, g)$ (b) versus wavelength, for various values of waveguide width w and coupling-gap width g .

In this expression, ΔL_i is the nominal length imbalance that corresponds with the desired phase delay $\Delta\phi_i$, according to

$$\Delta L_i = \frac{\lambda_0}{2\pi n_e^0} \Delta\phi_i. \quad (14)$$

The propagation constant $\beta(\lambda)$ is defined as

$$\beta(\lambda) = \frac{2\pi}{\lambda} n_e(\lambda) = \frac{2\pi}{\lambda} \left[n_e^0 - \frac{\lambda - \lambda_0}{\lambda_0} (n_g - n_e^0) \right], \quad (15)$$

where n_e^0 and n_g are respectively the effective index and group index of the SOI rib waveguide at the design wavelength λ_0 .

The complete MZL structure with S stages can then be described by the transmission matrix $\mathbf{M}(\lambda)$:

$$\mathbf{M}(\lambda) = \mathbf{C}_{S+1}(\lambda) \prod_{i=1}^S \mathbf{P}_i^{(A)}(\lambda) \mathbf{C}_i(\lambda). \quad (16)$$

Parameters for the submicron SOI rib waveguide

We used the commercially available eigenmode-expansion tool FimmWave to assess the model parameters n_e^0 , n_g , Γ and $L_C(\lambda, g)$. The simulated waveguide cross section for a DC is shown in fig. 5. A Sellmeier model [40] was used for evaluating the bulk refractive indices as function of wavelength, both for the Si core and the SiO₂ cladding. The coupling length $L_C(\lambda, g)$ was derived from the calculated effective indices $n_e^S(\lambda)$ and $n_e^A(\lambda)$ of the symmetric and antisymmetric supermode of the DC as

$$L_C(\lambda, g) = \frac{1}{2} \frac{\lambda}{n_e^S(\lambda) - n_e^A(\lambda)}. \quad (17)$$

$L_C(\lambda, g)$ was accurately fitted to the simulations using the expression

$$L_C(\lambda, g) = [a(\lambda - \lambda_0) + b] \exp \left[\frac{g}{c(\lambda - \lambda_0) + d} \right], \quad (18)$$

where a , b , c and d are fitting parameters, and λ and g are in micrometer. The results of the fitting are shown in table 2 and in Fig. 7, both for $n_e(\lambda)$ and $L_C(\lambda, g)$.

Table 2. Fitting parameters for a 450-nm-wide waveguide, with $\lambda_0 = 1.55 \mu\text{m}$.

| Parameter | Value | Parameter | Value | Parameter | Value |
|-----------|-------|-----------|--------------------|-----------|--------------------|
| Γ | 0.94 | a | -5.44 | c | 0.185 |
| n_e^0 | 2.37 | b | 3.53 μm | d | 0.15 μm |
| n_g | 4 | | | | |